Advanced Composites and Hybrid Materials (2023) 6:179
https://doi.org/10.1007/s42114-023-00755-9

RESEARCH

Double-phase engineering of cobalt sulfide/oxyhydroxide on metal-organic frameworks derived iron carbide-integrated porous carbon nanofibers for asymmetric supercapacitors

Debendra Acharya[1] · Tae Hoon Ko[1] · Roshan Mangal Bhattarai[2] · Alagan Muthurasu[1] · Taewoo Kim[1] · Syafiqah Saidin[3] · Jae-Shik Choi[4] · Kisan Chhetri[1] · Hak Yong Kim[1,3,5]

Received: 14 April 2023 / Revised: 22 August 2023 / Accepted: 16 September 2023 / Published online: 30 September 2023

Abstract

Designing advanced functional electrode materials with a tunable structure and multiphase/composition comprising a single metal via a one-step synthesis process for supercapacitor applications is challenging. Here, a dual-phase cobalt sulfide/cobalt oxyhydroxide ($Co_{1-x}S/HCoO_2$) hexagonal nanostructure on iron metal-organic framework (MIL-88A) derived iron carbide (Fe_3C) integrated porous carbon nanofibers (PCNFs) is synthesized using a wet-chemical curing technique. MIL-88A is integrated by a physical blending process into a PAN/PMMA polymer matrix during the PCNFs preparation process. The integrated MIL-88A-derived iron carbide nanomaterial contributes to improving the electrochemical performance of electrode materials by lowering the inherent resistance. The optimal ($Co_{1-x}S/HCoO_2$)-1@Fe_3C/PCNFs electrode exhibits a high specific capacitance of 1724 F g^{-1} at 1 A g^{-1} with an improved rate capability and exceptional cycling stability with 89.8% retention even after 10,000 cycles. These excellent electrochemical capabilities are predominantly attributed to the double-phase hybrid composites, which have a variety of abundant sites, a large active surface area, rapid electron and ion transport capability, and strong structural stability. A $Co_{1-x}S/HCoO_2$-1@Fe_3C/PCNFs//Fe_2O_3/NPC@PCNFs asymmetric supercapacitor (ASC) demonstrates excellent electrochemical energy storage behavior, with a maximum energy density of 65.68 Wh kg^{-1} at a power density of 752.7 W kg^{-1} and excellent cycling stability (90.3% capacitance retention after 10,000 charge-discharge cycles at a constant current density of 20 A g^{-1}). These electrochemical results indicate that this ASC outperforms previously reported asymmetric supercapacitors, showing that the heterophasic electrode ($Co_{1-x}S/HCoO_2$)-1@Fe_3C/PCNFs has the potential to be applied in supercapacitor devices.

Keywords Porous carbon nanofibers (PCNFs) · Metal-organic frameworks (MOFs) · MIL-88A · Cobalt sulfide/oxyhydroxide · Energy storage · Asymmetric supercapacitors (ASCs)

1 Introduction

In recent years, there has been a growing demand for efficient and sustainable energy storage systems to meet the increasing energy needs for various applications via solar cells, supercapacitors, and lithium-ion batteries [1–3]. The development of advanced energy storage systems plays a crucial role in achieving a sustainable energy future and addressing the challenges associated with energy storage, including efficiency, cost, and environmental impact [4–6].

✉ Kisan Chhetri
chhetrikisan88@jbnu.ac.kr

✉ Hak Yong Kim
khy@jbnu.ac.kr

[1] Department of Nano Convergence Engineering, Jeonbuk National University, Jeonju 561-756, Republic of Korea

[2] Department of Chemical Engineering, Jeju National University, Jeju-63243, Republic of Korea

[3] IJN-UTM Cardiovascular Engineering Centre, Institute of Human Centered Engineering, Universiti Teknologi Malaysia (UTM), Johor Bahru, Johor, Malaysia

[4] Department of Carbon Materials and Fiber Engineering, Jeonbuk National University, Jeonju 561-756, Republic of Korea

[5] Department of Organic Materials and Fiber Engineering, Jeonbuk National University, Jeonju 561-756, Republic of Korea

Therefore, nowadays researchers are focused to investigate and optimize the performance of energy storage devices such as solar cells, supercapacitors, fuel cells, air batteries, and lithium-ion batteries to contribute to the advancement of clean and efficient energy for future technologies [7, 8]. Among various energy storage systems, supercapacitors (SCs) are emerging as a type of energy storage technology due to their high levels of safety, rapid charge-discharge rate, prolonged cycle life, high power density, and excellent cycling stability [9, 10]. However, their low energy density and commercial problems are major barriers to their widespread practical application [11–13]. As a result, research scientists are focusing on developing advanced and cost-effective electrode materials with unique nanostructures and morphologies that can store a great amount of energy and are very useful for a wide range of applications, including electric vehicles (EVs) [14, 15]. Currently, binder-free strategies are being used for the preparation of electrodes to reduce active material exfoliation. This is because binders increase the dead mass of active materials and diminish the overall electrochemical performance [16–18]. The development of binder-free advanced functional electrode materials with good electrochemical performance is also a challenging issue for next-generation supercapacitor applications [19–21]. In recent years, electrospun carbon nanofibers have garnered considerable attention as potential candidates for constructing functional binder-free electrode materials [22–26]. However, these materials must possess a high surface area, high electrical conductivity, robust electrochemical stability, and open porosity to serve as high-performance electrode materials [27–29]. Electrospun porous carbon nanofibers (PCNFs) have the potential to possess the aforementioned characteristics [30, 31]. As well, several attempts are being used to enhance the overall electrochemical energy storage performance of electrospun carbon nanofiber-based electrodes [31, 32]. The integration of various additives, such as transitional metal oxides/phosphides/sulfides/selenides, conductive polymers, MXenes, and nanomaterials derived from metal-organic frameworks (MOFs), is a convenient approach for enhancing the overall performance of electrode materials [32–36]. Specifically, the integration of nanomaterials derived from metal-organic frameworks (MOFs) is the most remarkable and beneficial technique [37–39]. Typically, MOFs are nanomaterials with a high surface area and numerous nanopores in which metal ions or clusters are bound inside a specific framework of organic ligands [40, 41]. The high surface area and pores with active metal nodes of MOF-derived nanomaterials increase the electrochemical activity, mechanical stability, and ionic conductivity of carbon nanofibers, which also lowers the interfacial resistance of carbon nanofiber–based electrodes [42–44]. Furthermore, MOF-derived nanomaterial-embedded PCNFs have improved electrolyte diffusion rates, leading to enhanced overall electrochemical performance [45, 46].

Electrode materials based on transition metals and their derivatives have ideal faradaic performance and exhibit high electrochemical performance [47]. Therefore, pseudocapacitive materials, including metal oxides [48], hydroxides [49], oxyhydroxides [50], phosphides [32, 51], and sulfides [52], are being utilized to prepare electrode materials for energy applications. Among these, transition metal sulfides (TMSs) are advanced functional electrode materials for supercapacitors. TMSs have received the most attention among the various electrode materials because of their more abundant redox sites, higher conductivity, and higher theoretical capacitance than those of other electrode materials [53–55]. However, a low specific capacitance and short cycle life are typical drawbacks of metal sulfides, rendering them unsuitable for use in high-performance supercapacitors [56]. The integration of TMSs with conductive carbonaceous materials such as porous carbon fibers is the best way to prepare stable advanced functional electrode materials with improved capacitance and energy density for supercapacitor applications [46]. However, only the surface region materials actively participate in the faradaic mechanism even after hybridization with conductive carbon-based materials [57]. As a result, it is essential to research optimal functional materials and then precisely tune and design their microstructures utilizing distinctive components [58].To increase the usage of bulk pseudocapacitive materials and improve the efficiency of charge and ion transfer, several techniques are being employed to engineer single-metal heterophasic nanomaterials with controlled morphology on low-resistivity substrates [59]. Multiphasic nanomaterials provide more redox sites for ion and electron movement, which can increase the surface electrochemical behavior for improved electrochemical performance. Therefore, designing and engineering nanomaterials with unique nanostructures on MOF-derived nanomaterial-integrated porous carbon nanofibers as a low-resistivity substrate is an effective method for enhancing electrochemical performance [60, 61].

This work first involves the hydrothermal synthesis of MIL-88A, followed by the blending of the synthesized MIL-88A nanoparticles with a PAN/PMMA polymer solution. A high-voltage electrospinning technique is then employed to prepare nanofiber mats. MIL-88A-integrated nanofibers via low-temperature stabilization and high-temperature carbonization processes are employed to generate Fe_3C/PCNFs. The double-phase ($Co_{1-x}S/HCoO_2$) is designed on the surface of Fe_3C/PCNFs by a one-step chemical curing process under fixed temperature and pressure. To date, this sort of hybrid composite has not been reported for energy applications. The low-electronegative sulfur present in the prepared electrode ($Co_{1-x}S/HCoO_2$)-1@Fe_3C/PCNFs enhances the redox sites and improves conductivity. The nonstoichiometric cobalt

oxyhydroxide ($HCoO_2$) present in the engineered phase has a greater amount of cobalt in the Co^{3+} oxidation state [62]. Therefore, the optimal electrode ($Co_{1-x}S/HCoO_2$)-1@Fe_3C/PCNFs exhibits low internal resistance and excellent cycling life with remarkable specific capacitance. Moreover, we combine ($Co_{1-x}S/HCoO_2$)-1@Fe_3C/PCNFs and Fe_2O_3/NPC@PCNFs as a positive and negative electrode, respectively, to construct an asymmetric supercapacitor (ASC) (($Co_{1-x}S/HCoO_2$)-1@Fe_3C/PCNFs//Fe_2O_3/NPC@PCNFs) to offer a sustainable energy option. The details of the negative electrode material (Fe_2O_3/NPC@PCNFs) preparation method and the electrochemical data are presented in our previously published work [63]. The fabricated ASC device exhibits remarkable cyclic stability, high specific capacity, and high energy density. The double-phase nanomaterials ($Co_{1-x}S/HCoO_2$) and integrated nanoporous materials (Fe_3C derived from MIL-88A into PCNFs) create stable active sites for charge and ion transfer within the advanced electrode materials. Similarly, the porosity of the advanced electrode materials ($Co_{1-x}S/HCoO_2$)-1@Fe_3C/PCNFs slows the movement of electrolytes within the electrode and acts as electrolyte reservoirs to increase the charge storage capacity during the electrochemical reaction between the electrode and electrolyte.

2 Experimental

The required materials and preparation of MIL-88A are explained in the Supporting Information file in Sections 1.1 and 1.2.

2.1 Preparation of the Fe_3C-integrated porous carbon nanofibers (Fe_3C/PCNFs)

PAN and PMMA in mass ratios (90:10) were dissolved in DMF and stirred for 6 h at room temperature to make the spinning solution. After that, a certain amount of MIL-88A was blended in the PAN/PMMA matrix with the help of a magnetic stirrer. Then, under the typical conditions (an applied voltage of 17 kV, a distance between the needle and collector of 15 cm, and a solution feeding rate of 1 mL h^{-1}), the electrospinning of the prepared solution was carried out to prepare the MIL-88A/PAN/PMMA nanofiber mat. The MIL-88A/PAN/PMMA nanofiber mat was initially vacuum-dried at 60 °C for 12 h. The resulting MIL-88A/PAN/PMMA nanofiber mat was then stabilized at 250 °C at a rate of 2 °C min^{-1} for 1 h and carbonized at 900 °C at a rate of 1 °C min^{-1} for 1 h under an N_2 atmosphere. Finally, a black MIL-88A-derived Fe_3C-integrated nanofiber mat was developed. The synthesized products were labeled as Fe_3C/PCNFs. Similarly, PCNFs were prepared by electrospinning of 90:10 PAN and PMMA solution using same conditions of Fe_3C/PCNFs.

2.2 Synthesis of $Co_{1-x}S/HCoO_2$@Fe_3C/PCNFs

The synthesized Fe_3C/PCNFs mat was treated hydrothermally in a 50-mL Teflon tube containing 1 mmol $Co(NO_3)_2.6H_2O$ and 1 mmol NH_4N_2S in a 40 mL ammoniated solution. The ammoniated solution was prepared by mixing liquid ammonia and distilled water in an equal ratio. The autoclave was heated to 150 °C for 10 h. After naturally cooling to room temperature, the nanomaterials containing Fe_3C/PCNFs mat were taken out from the Teflon tube, washed, and vacuum dried for 12 h at 60 °C. The resulting product was labeled as ($Co_{1-x}S/HCoO_2$)-1@Fe_3C/PCNFs. For comparison, different concentrations of $Co(NO_3)_2.6H_2O$, such as 0.5 and 1.5 mmol, were used, and the corresponding products were labeled as($Co_{1-x}S/HCoO_2$)-0.5@Fe_3C/PCNFs and ($Co_{1-x}S/HCoO_2$)-1.5@Fe_3C/PCNFs, respectively. Furthermore, $Co_{1-x}S/HCoO_2$@PCNFs were prepared using the same conditions as those for ($Co_{1-x}S/HCoO_2$)-1@ Fe_3C/PCNFs, but instead of the Fe_3C/PCNFs mat, the PCNFs mat was used.

2.3 Electrochemical measurements

All electrochemical measurements, including cyclic voltammetry (CV), galvanostatic charge-discharge (GCD), and electrochemical impedance spectroscopy (EIS) test were recorded at room temperature in an electrochemical workstation using the VersaSTAT-4 instrument in both 3- and 2-electrode systems. In the 3-electrode system, the working electrode consisted of the prepared materials, while the reference electrode was Hg/HgO, and the counter electrode was a platinum mesh. For all electrochemical characterization, a 3 M KOH solution was utilized as the electrolyte. Detailed information regarding the electrochemical measurements and mass/charge balancing during the fabrication of the ASC for the 2-electrode system can be found in Section 1.4 of the supporting information file.

3 Results and discussion

3.1 Synthesis and morphological analysis

The synthesis process of the ($Co_{1-x}S/HCoO_2$)-1@Fe_3C/PCNFs double-phase hexagonal nanomaterials is demonstrated in Fig. 1, and the in-depth experimental details regarding the synthesis are discussed in Sections 1 and 2 in the supporting information file and manuscript, respectively. The rice grain-shaped MIL-88A (Fig. S1(a, b)) nanomaterials are prepared by a hydrothermal process. The

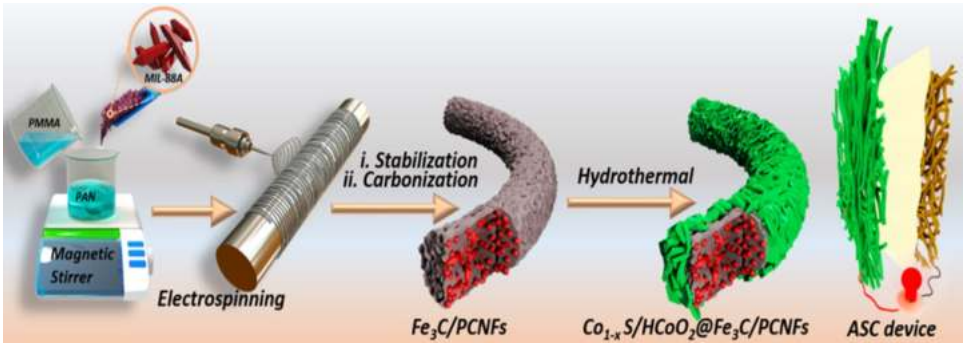

Fig. 1 Schematic diagram of the fabrication process of positive electrode materials for the ASC device

thermally decomposable polymethyl methacrylate (PMMA) at high temperature is used to generate the pores and roughness of the polyacrylonitrile (PAN) nanofiber surface, as shown in Fig. S1c, facilitating the sustainable growth of $Co_{1-x}S/HCoO_2$ on the outer surface. Figure S1d shows the TEM images of the prepared Fe_3C/PCNFs, in which a large amount of MIL-88A-derived Fe_3C nanomaterial is distributed within the porous carbon nanofiber. The integrated Fe_3C derived from MIL-88A in the porous carbon nanofibers provides a much higher, continuous, and fast electronic conductivity (Table S1:measurement of conductivity) and enhances the intrinsic electrochemical activities of the electrode materials by shortening the pathways for improved faradaic reactions at the electrolyte-electrode surface. The large organic ligands thiourea and ammonia solution are used during a one-step solvothermal process to engineer a double-phase ($Co_{1-x}S/HCoO_2$) on the surface of the substrate (Fe_3C/PCNFs). The FE-SEM images of ($Co_{1-x}S/HCoO_2$)-0.5@Fe_3C/PCNFs, ($Co_{1-x}S/HCoO_2$)-1.5@Fe_3C/PCNFs, $Co_{1-x}S/HCoO_2$@PCNFs, and ($Co_{1-x}S/HCoO_2$)-1@Fe_3C/PCNFs are displayed in Fig. S2 (supporting information file) and Fig. 2. Among the prepared electrode materials, ($Co_{1-x}S/HCoO_2$)-1@Fe_3C/PCNFs is selected for detailed studies due to the uniform growth of $Co_{1-x}S/HCoO_2$ nanomaterials on Fe_3C/PCNFs.

The FE-SEM images of ($Co_{1-x}S/HCoO_2$)-1@Fe_3C/PCNFs) shown in Fig. 2a–c demonstrate the intimate contact between the hexagonal $Co_{1-x}S/HCoO_2$ nanomaterials and the Fe_3C/PCNFs, improving the overall stability and facilitating the kinetics of ions and electrons at the electrode/electrolyte interface. The EDX analysis (Fig. 2d) and elemental mapping analysis (Fig. 2e, e_1, e_2, e_3) demonstrate the uniform distribution of C, O, S, and Co on the outer surface of Fe_3C/PCNFs.

The phase compositions and successful synthesis of the electrode material are verified by using X-ray diffraction (XRD). The XRD pattern of the prepared MIL-88A nanomaterials is displayed in Fig. S3a. The large peak at approximately 24° (Fig. S3b) corresponds to the graphitic carbon plane (002) of the carbonized PCNFs. However, this peak is observed to be narrower and sharper in the XRD pattern of Fe_3C/PCNFs, which is due to the formation of Fe_3C from integrating MIL88A into the PCNFs matrix during carbonization. The specific peaks corresponding to Fe_3C are observed in the XRD analysis (Fig. S3b), indicating the high level of integrated MIL-88A is converted into Fe_3C by a high-temperature thermal treatment process. The XRD pattern of the ($Co_{1-x}S/HCoO_2$)-1@Fe_3C/PCNFs is presented in Fig. 2f. The observed diffraction peaks at 30.51°, 35.17°, 46.70°, 54.20°, and 62.32°, corresponding to the hexagonal $Co_{1-x}S$ (PDF#42-0826) planes (100), (101), (102), (100), (110), (110), and (103), respectively. Similarly, the (003), (101), (012), (006), (110), and (113) planes of hexagonal $HCoO_2$ (PDF#73-0497) are represented by diffraction peaks at 20.2, 37.01, 38.9, 41.1, 65.4, and 69.2°, respectively. The XRD graphs of the ($Co_{1-x}S/HCoO_2$)-0.5@Fe_3C/PCNFs, ($Co_{1-x}S/HCoO_2$)-1.5@Fe_3C/PCNFs, and $Co_{1-x}S/HCoO_2$@PCNFs, as presented in Fig. S3c (in the Supporting Information file), exhibit the similar characteristic peak of hexagonal $Co_{1-x}S$ and particular hexagonal $HCoO_2$. The TEM images presented in Fig. 2g–i exhibit the interconnected structure of $Co_{1-x}S/HCoO_2$ nanomaterials on the surface of Fe_3C/PCNFs, which is consistent with the structure observed in the FE-SEM image. The presence of various lattice phases of two different compounds, which can efficiently facilitate charge transfer, is confirmed by the HR-TEM image. The HR-TEM image of ($Co_{1-x}S/HCoO_2$)-1@Fe_3C/PCNFs demonstrated in Fig. 2j shows lattice fringes with interlayer distances of 0.29 and 0.19 nm, which correspond to the $Co_{1-x}S$ (100) and (102) planes (Fig. 2j_1, j_2), respectively, while the lattice spacings of 0.18 and 0.43 nm correspond to the $HCoO_2$ (015) and (003) planes (Fig. 2j3, j4), respectively. The XRD and TEM findings confirm that the synthesized ($Co_{1-x}S/HCoO_2$)-1@Fe_3C/PCNFs contains both $Co_{1-x}S$ and $HCoO_2$, suggesting the efficient synthesis of double-phase nanomaterials on the Fe_3C/PCNFs surface.

The performance of metal-based electrodes is greatly influenced by their surface chemistry because the nucleation process that occurs during the fabrication of electrode materials is surface-dominated. The X-ray photoelectron spectroscopy (XPS) general survey scan indicates the presence of oxygen, sulfur, and cobalt in the nanoparticles on

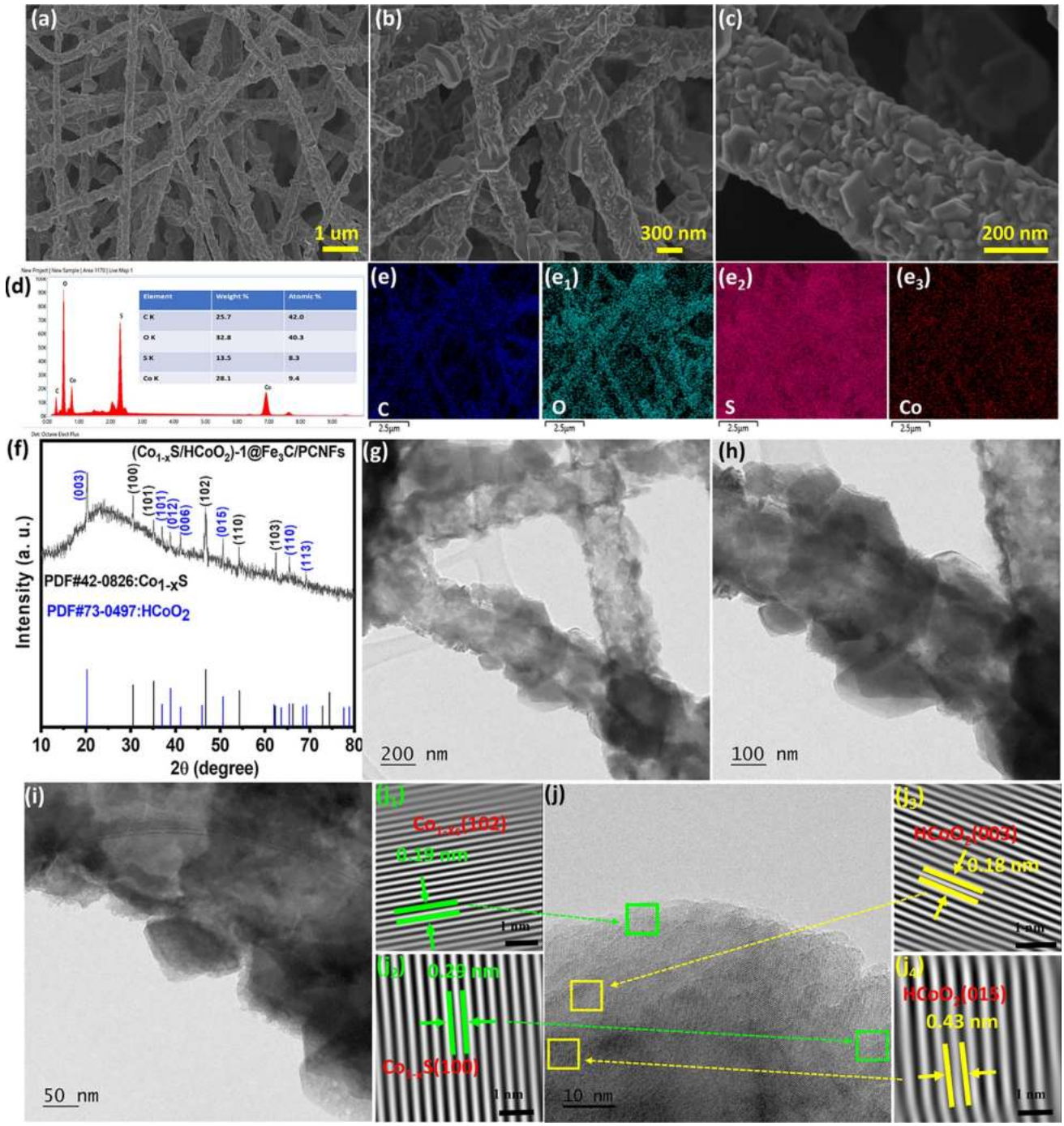

Fig. 2 Morphological characterizations of $(Co_{1-x}S/HCoO_2)$-1@Fe_3C/PCNFs. **a**, **b**, **c** FE-SEM images at different magnifications, **d** EDX analysis, and **e**, $\mathbf{e_1}$, $\mathbf{e_2}$, $\mathbf{e_3}$ color mapping for elemental analysis. **f–i** XRD patterns and TEM images of $(Co_{1-x}S/HCoO_2)$-1@Fe_3C/PCNFs, respectively, and **j** HR-TEM and IFFT images ($\mathbf{j_1}$, $\mathbf{j_2}$, $\mathbf{j_3}$, $\mathbf{j_4}$) used for calculating the d-spacing of the synthesized materials

the Fe_3C/PCNFs surface (Fig. 3a), which is analogous to the results obtained from the EDX analysis and color mapping of FE−SEM. As shown in Fig. 3b, the XPS Co 2p spectra of $(Co_{1-x}S/HCoO_2)$-1@Fe_3C/PCNFs exhibits two spin-orbit doublets, Co $2p_{3/2}$ and Co $2p_{1/2}$, with low energy peak of 781.8 eV and a high energy peak of 797.9 eV, respectively. The satellite peaks at 785.5 and 802.4 eV correspond to the binding energy of Co^{2+}, and the low-intensity peak at 778.1 eV indicates that there is an increase in the electron density of S, and Co atoms can accept electrons from S atoms, demonstrating the specific chemical interaction between S and Co [64]. The peaks observed at 161.83 eV

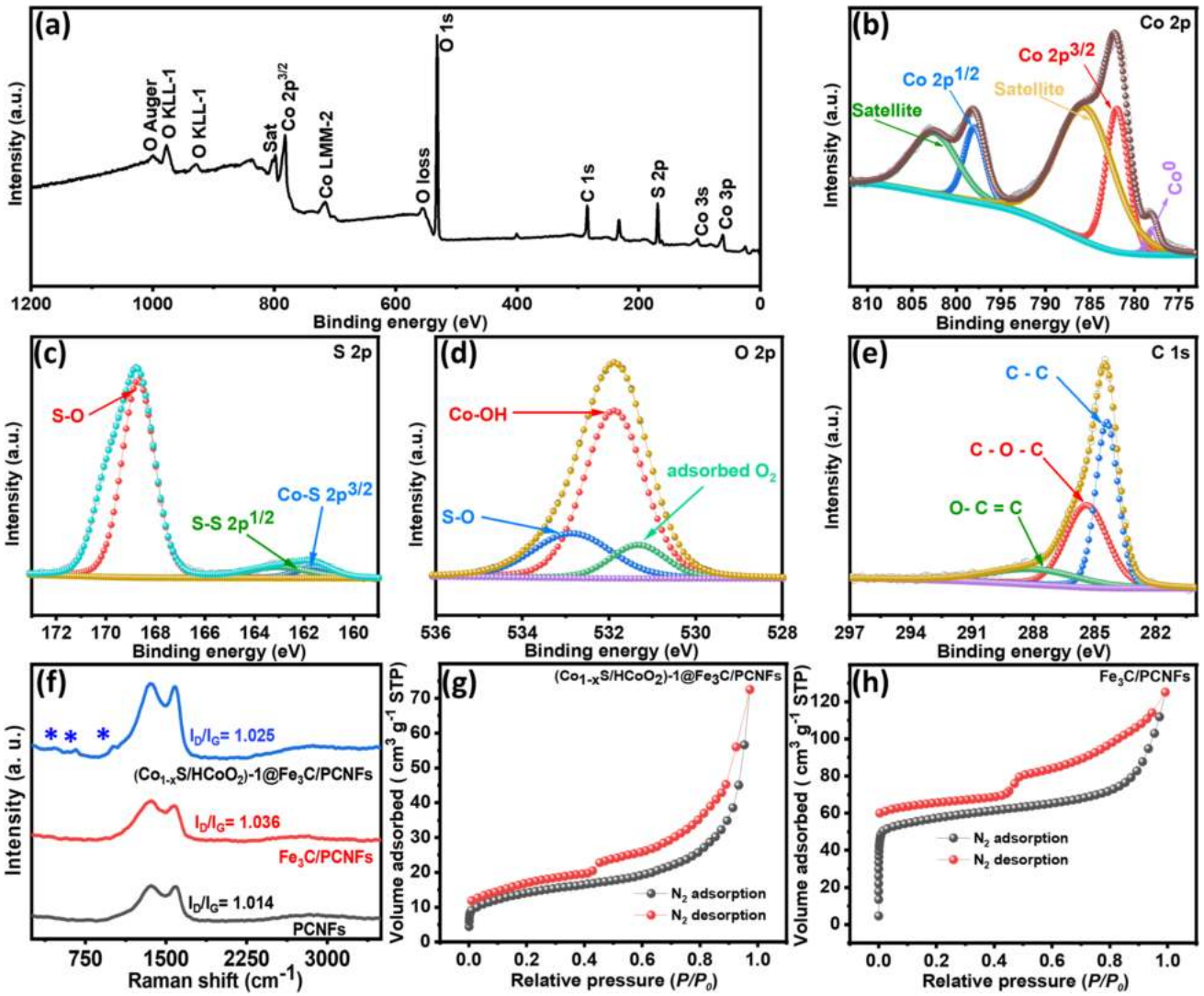

Fig. 3 **a** XPS survey spectrum of $(Co_{1-x}S/HCoO_2)$-1@Fe_3C/PCNFs at low-resolution, deconvoluted high-resolution XPS **b** Co 2p, **c** S 2p, **d** O 1s, and **e** C 1s spectra of $(Co_{1-x}S/HCoO_2)$-1@Fe_3C/PCNFs. **f** Raman spectra of $(Co_{1-x}S/HCoO_2)$-1@Fe_3C/PCNFs, Fe_3C/PCNFs, and PCNFs, and **g**, **h** BET isotherms of Fe_3C/PCNFs and $(Co_{1-x}S/HCoO_2)$-1@Fe_3C/PCNFs

and 163.05 eV in the high-resolution scan of the fitted S 2p spectra (Fig. 3c) indicate the presence of a Co–S bond and that there are relatively more S atoms than Co present in $Co_{1-x}S$ [65]. Furthermore, the emergence of a satellite peak at 169.94 eV is attributed to high valance owing to the surface oxidation of sulfur [66]. The XPS spectra obtained for O 1s (Fig. 3d) have two deconvoluted peaks at 531.8 and 531.3 eV, indicating the formation of the M–OH bond and S–O bond related to sulfate groups. The observed split peak at 532.85 eV corresponds to the adsorbed oxygen atom on the surface [67]. The high-resolution C 1s scan (Fig. 3e) shows prominent peaks of C–C and C–O–C at 284.3 eV and 285.6 eV, as well as a decrease in the intensity of the peaks of C = C–O at 288.3 eV [68]. Furthermore, the XPS measurements of Fe_3C/PCNFs and pristine PCNFs are presented in Fig. S4 of the supporting information file. The high-resolution spectrum of Fe 2p (Fig. S4b) shows peaks at 710.1 eV and 723.6 eV, corresponding to the Fe $2p_{3/2}$ and Fe $2p_{1/2}$ states of Fe_3C, respectively. These XPS measurements confirm the integration of Fe_3C within the interlayer of PCNFs [69]. These findings, which are in good agreement with the XRD and TEM analyses, confirm the successful formation of $(Co_{1-x}S/HCoO_2)$ on the Fe_3C/PCNFs surface.

Furthermore, Raman spectroscopy is used for the PCNFs, Fe_3C/PCNFs, and $(Co_{1-x}S/HCoO_2)$-1@Fe_3C/PCNFs to characterize the detailed bonding structure of these carbon nanomaterials. As shown in Fig. 3f, the two prominent Raman peaks observed for all of the samples are at ~ 1352 and 1583 cm^{-1}, which are associated with graphitic (G band) and disordered (D band) carbon, respectively. The I_D/I_G band

intensity ratio of Fe_3C/PCNFs (1.036) is higher than that of PCNFs (1.014), indicating that the integration of MIL-88A-derived Fe_3C introduced more defects in PCNFs. These findings indicate that the Fe_3C/PCNFs composite exhibits the highest degree of microstructure order and achieves a more graphitic structure, resulting in enhanced electrical conductivity compared to the PCNFs matrix. The I_D/I_G band intensity ratio of $Co_{1-x}S/HCoO_2$@Fe_3C/PCNFs (1.025) remains comparable to that of Fe_3C/PCNFs even after a significant amount of $Co_{1-x}S$ and $HCoO_2$ nanomaterials are attached to the Fe_3C/PCNFs surface. Furthermore, nitrogen adsorption-desorption (BET analysis) is used to investigate the specific surface area and porosity of the Fe_3C/PCNFs and $(Co_{1-x}S/HCoO_2)$-1@Fe_3C/PCNFs electrode materials. As shown in Fig. 3g, h, both as-prepared samples exhibit a typical adsorption-desorption isotherm. The BET surface area of Fe_3C/PCNFs is 231.5 $cm^2\ g^{-1}$, which is much higher than the value of 61.2 $cm^2\ g^{-1}$ for the $(Co_{1-x}S/HCoO_2)$-1@Fe_3C/PCNFs electrode material. The decrease in specific surface area after the growth of $Co_{1-x}S/HCoO_2$ nanomaterials indicates the good and uniform distribution of nanomaterials on the surface of Fe_3C/PCNFs. The BJH model was used to determine the average pore size of the $(Co_{1-x}S/HCoO_2)$-1@Fe_3C/PCNFs electrode materials, which is mostly in the 5.8 ~ 16.7 nm range (Fig. S5). The BET texture properties of the Fe_3C/PCNFs and $(Co_{1-x}S/HCoO_2)$-1@Fe_3C/PCNFs are summarized in Table S2. The accessible surface area and pore distribution allow for an improved contact area between the electrode material and electrolyte, resulting in abundant active sites and promoting ion penetration and diffusion [70, 71].

3.2 Electrochemical performance of the prepared electrodes in a 3-electrode system

The overall electrochemical performance of $(Co_{1-x}S/HCoO_2)$-0.5@Fe_3C/PCNFs, $(Co_{1-x}S/HCoO_2)$-1@Fe_3C/PCNFs, $(Co_{1-x}S/HCoO_2)$-1.5@Fe_3C/PCNFs, and $Co_{1-x}S/HCoO_2$@PCNFs is tested using a platinum electrode as the counter electrode and Hg/HgO as the reference electrode (potential window: 0–0.5 V vs. Hg/HgO), and high-ionic-conductivity KOH as the electrolyte. The cyclic voltammetry (CV) curves and galvanostatic charge-discharge (GCD) curves of all as-prepared electrodes at 50 mV s^{-1} and 3 A g^{-1} respectively, are shown in Fig. 4a, b. The $(Co_{1-x}S/HCoO_2)$-1@Fe_3C/PCNFs electrode material has a more rectangular CV curve with a larger integrated area than the $(Co_{1-x}S/HCoO_2)$-0.5@Fe_3C/PCNFs and $(Co_{1-x}S/HCoO_2)$-1.5@Fe_3C/PCNFs electrode materials. The specific capacitance of the synthesized electrode materials is calculated using Eq. S1 (supporting information file). As shown in Fig. 4c, the $(Co_{1-x}S/HCoO_2)$-1@Fe_3C/PCNFs has a capacitance of 1559 F g^{-1} at 3 A g^{-1}, which is 1.52 and 1.73 times greater than that of the $(Co_{1-x}S/HCoO_2)$-0.5@Fe_3C/PCNFs and $(Co_{1-x}S/HCoO_2)$-1.5@Fe_3C/PCNFs, respectively. The high capacitance of the

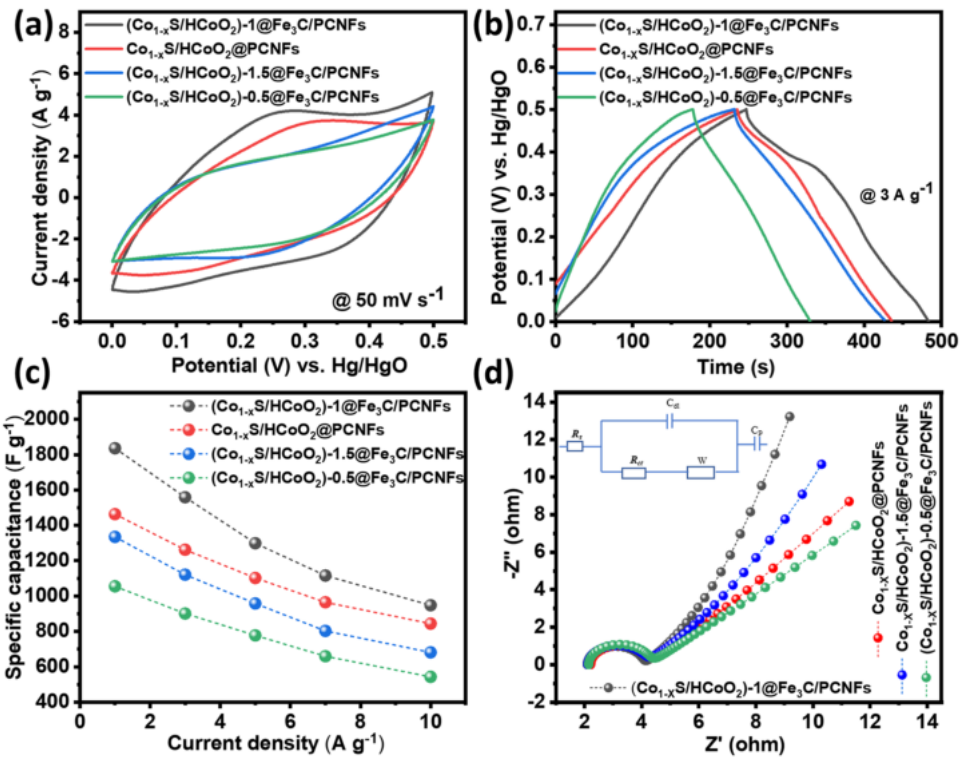

Fig. 4 A comparative study of all prepared electrode materials. **a** CV curves at a 50 mV s^{-1} scan rate, **b** GCD curves at a 3 A g^{-1} current density, **c** plot of the specific capacitance and current densities, and **d** electrochemical impedance spectroscopy (EIS) plot with the equivalent circuit diagram inset

prepared electrode material is due to the uniform interconnection of nanomaterials on the substrate materials. Similarly, the capacitance of $(Co_{1-x}S/HCoO_2)$-1@Fe_3C/PCNFs is 1.23 times greater than that of $Co_{1-x}S/HCoO_2$@PCNFs due to the presence of Fe_3C derived from integrating MIL-88A in the carbon nanofiber matrix. Figures S6, S7, and S8 display the CV curves at different scan rates, the GCD curves at different current densities, and the specific capacitance values at different current densities of the $(Co_{1-x}S/HCoO_2)$-0.5@Fe_3C/PCNFs, $(Co_{1-x}S/HCoO_2)$-1.5@Fe_3C/PCNFs, and $Co_{1-x}S/HCoO_2$@PCNFs. The specific capacitances of all the electrodes along with their rate performance, which is calculated using the integrated area under the GCD discharge curve, are listed in Table S3 (supporting information file). The electrode material $(Co_{1-x}S/HCoO_2)$-1@Fe_3C/PCNFs also demonstrates the best rate performance even at high current density with high capacitance retentions. EIS is performed under open-circuit conditions from 10^5 to 0.5 Hz to study the enhanced electrochemical behavior of all the as-synthesized electrode materials. The fitted Nyquist plots of all synthesized electrodes, as shown in Fig. 4d, demonstrate a straight line in low-frequency regions and a semicircle in high-frequency regions. The shape and diameter of the semicircle in the high-frequency curve represent the charge transfer resistance (R_{ct}) and the bulk resistance (R_s) of the electrodes, respectively. The $(Co_{1-x}S/HCoO_2)$-1@Fe_3C/PCNFs electrode displays a vertical line with a large slope in the low-frequency region and a semicircle with a small diameter in the high-frequency region. This indicates that the integrated MIL-88A-derived Fe_3C optimized the capacitive behavior of the electrode for improved electrochemical activity. The values of R_s and R_{ct} of all prepared electrode materials are summarized in Table S4 (supporting information file). Based on the comparative analysis, we select $(Co_{1-x}S/HCoO_2)$-1@Fe_3C/PCNFs as the optimum electrode material compared to other prepared electrodes for further electrochemical experiments.

Figure 5a shows the CV profile of $(Co_{1-x}S/HCoO_2)$-1@Fe_3C/PCNFs within a 0 to 0.5 V potential window at various scan rates. The rectangular CV profiles with a pair of broad redox peaks imply an enhanced reversible faradaic reaction with a lesser degree of capacitive behavior and less resistance. The broad redox peaks observed on both anodic and cathodic sides suggest that the energy storage mechanism is mostly dependent on redox processes. In the $(Co_{1-x}S/HCoO_2)$-1@Fe_3C/PCNFs electrode, the $Co_{1-x}S$ hexagonal phase and the $HCoO_2$ phase are both electroactive species that contribute to energy storage in the alkaline electrolyte. Reversible redox reactions of $Co^{2+}/Co^{3+}/Co^{4+}$ are responsible for the redox peaks in the CV curves. The electrochemical redox reactions that occur during the charge storage process in an alkaline electrolyte can be described by the following reactions [72]:

$$Co_{1-X}S + OH^- \leftrightarrow Co_{1-X}SOH + e^-$$

$$Co_{1-X}SOH + OH^- \leftrightarrow Co_{1-X}S\,O + e^-$$

$$HCoO_2 + OH^- \leftrightarrow CoO_2 + H_2O + e^-$$

As the scan rate increases, the reduction and oxidation peaks of the $(Co_{1-x}S/HCoO_2)$-1@Fe_3C/PCNFs electrode shift towards their respective cathodic and anodic sides. Importantly, the shape of the curve remains unchanged. This observation highlights the electrode's remarkable capability for current charge-discharge cycling and the excellent reversibility of the redox reaction. Figure 5b demonstrates the GCD curves of $(Co_{1-x}S/HCoO_2)$-1@Fe_3C/PCNFs at different current densities within a fixed potential range of 0 to 0.5 V. The almost symmetric GCD curves of $Co_{1-x}S/HCoO_2$ indicate a high charge-discharge coulombic efficiency and low polarization. As illustrated in Fig. 5c, the specific capacitance is determined to be 1724 F g^{-1}, 1559 F g^{-1}, 1336 F g^{-1}, 1189 F g^{-1}, and 1019 F g^{-1} at current densities of 1 A g^{-1}, 3 A g^{-1}, 5 A g^{-1}, 7 A g^{-1}, and 10 A g^{-1}. The decrease in the specific capacitance of electrode materials with increasing current density is related to more difficult electrolyte penetration and diffusion, the inadequate faradic reaction of active materials, and the resistance at high current densities. Furthermore, it can be observed that $(Co_{1-x}S/HCoO_2)$-1@Fe_3C/PCNFs still has a respectable rate capability and coulombic efficiency. The electrode $(Co_{1-x}S/HCoO_2)$-1@Fe_3C/PCNFs retains approximately 59.1% of its capacitance and has 91.6% coulombic efficiency at 10 A g^{-1}.

The cyclic GCD stability test (shown in Fig. 5d) is used to investigate the lifespan and stability of $(Co_{1-x}S/HCoO_2)$-1@Fe_3C/PCNFs. After 10,000 GCD stability cycles, the electrode $(Co_{1-x}S/HCoO_2)$-1@Fe_3C/PCNFs retains 86.7% capacitance and 91.3% coulombic efficiency. Interestingly, the specific capacitance of the $(Co_{1-x}S/HCoO_2)$-1@Fe_3C/PCNFs electrode is on par with that of previously reported transition metal-sulfide and hydroxide-based electrodes (Table S5, supporting information file). The post-electrochemical characterization studies confirm the robust stability of the electrode material. Examination of the FE-SEM images of $(Co_{1-x}S/HCoO_2)$-1@Fe_3C/PCNFs electrodes after the electrochemical test (Fig. S9) reveals preserved morphologies without noticeable deformations. The good cycle stability with significant capacitance is due to the uniform growth and highly interconnected hexagonal porous nanostructure of the Fe_3C-integrated porous carbon nanofibers (Fe_3C/PCNFs). The integrated MIL-88A-derived Fe_3C considerably boosts the electrical conductivity

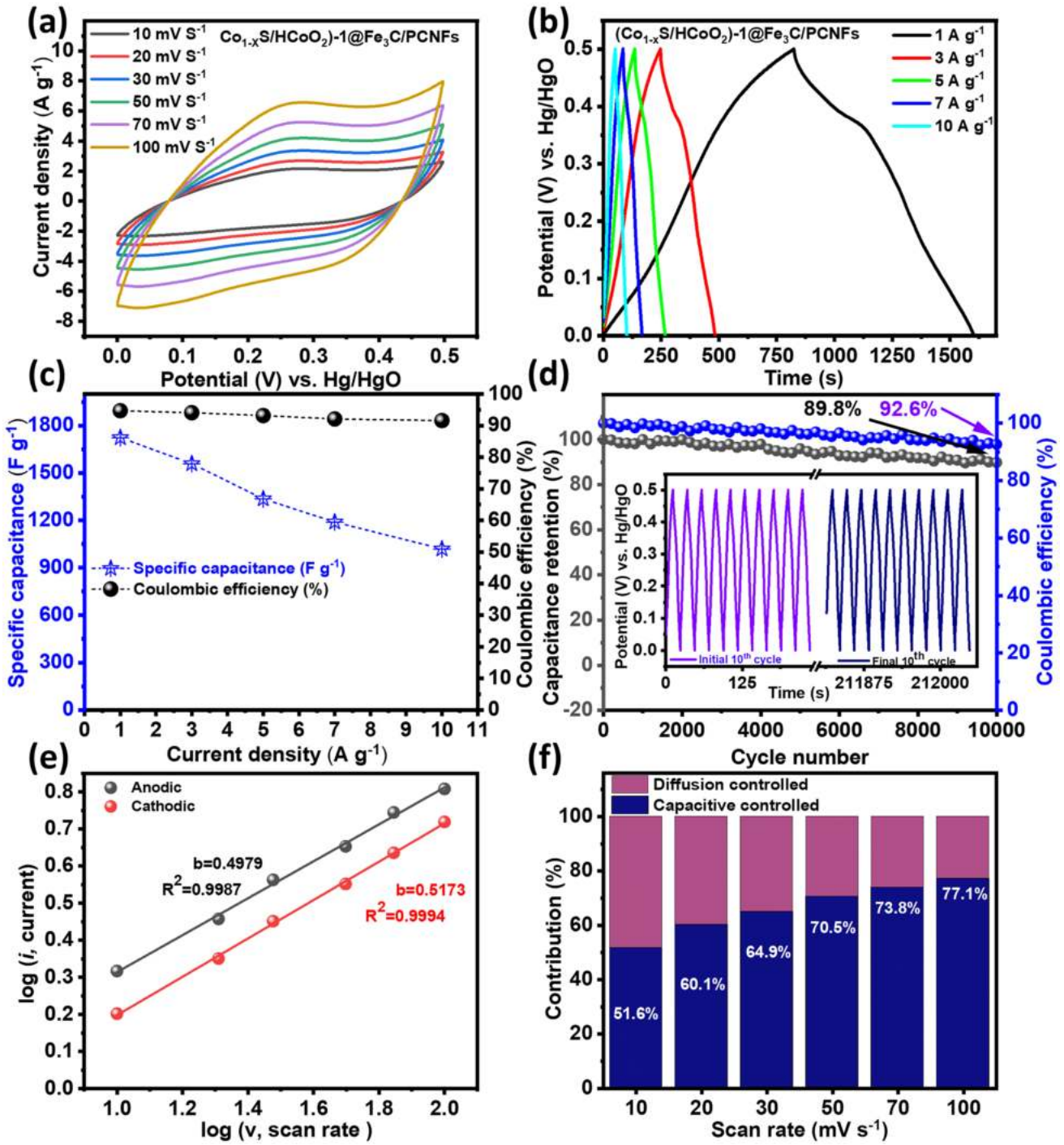

Fig. 5 Electrochemical characterization of $(Co_{1-x}S/HCoO_2)$-1@Fe_3C/PCNFs. **a**, **b** CV and GCD curves recorded at various scan rates and current densities, respectively, **c** specific capacitance and coulombic efficiency as a function of current density, **d** specific capacitance and coulombic efficiency as a function of cycle number (inset: initial and final 10 cycles of 10,000 charge-discharge cycles), **e** fitting plots between log (i) current and log (v) scan rate at various peak currents, and **f** normalized capacitance contribution at various scan rates

of the composite electrode, resulting in the high current responsiveness of the electrode and contributing to the enhancement of the electrode material life cycle. Fig. S10 depicts the Nyquist plots of the $(Co_{1-x}S/HCoO2)$-1@Fe_3C/PCNFs electrode before and after the cycling stability test. Before the cycling stability test, the R_s and R_{ct} values of the electrode material are 2.12 and 1.92, respectively. After the stability test, the R_s and R_{ct} values slightly increase to 2.44

and 2.08, respectively, indicating stability with consistent conductivity. Furthermore, owing to the high current density employed, the minor increase in intrinsic resistance of the electrode is due to an increase in diffusion route length caused by the repetitive cycling effect.

The kinetics and energy storage mechanism of the ($Co_{1-x}S/HCoO_2$)-1@Fe_3C/PCNFs cathode are explored further using the power-law equation as presented in section 1.5 of the supporting information file. When the *b* value is 0.5, the electrode reaction is controlled by diffusion; however, when the *b* value is 1, the capacitive surface reaction dominates the electrode reaction. Figure 5e shows that the *b* values for the ($Co_{1-x}S/HCoO_2$)-1@Fe_3C/PCNFs oxidization and reduction peaks are 0.49 and 0.51, respectively, indicating a rapid diffusion-controlled charge storage mechanism. In addition, by using the Dunn approach presented in Section 1.5 of the supporting information file, the contributions of potential-dependent capacitive and diffusion-controlled processes to the total charge storage are also determined. As shown in Fig. 5f, the capacitive and diffusion contribution is calculated to be 51.6% and 48.4%, respectively, of the total charge stored at a 10 mV s^{-1} scan rate. This demonstrates that both diffusion and surface capacitive processes play significant roles in controlling the charge storage mechanism. Furthermore, the observed relatively fast kinetics during charging and discharging suggest efficient energy storage and release. The capacitive contribution gradually increases to 77.1% and the diffusion contribution gradually decreases to 22.9% at a high scan rate of 100 mV s^{-1}. The percentage contribution of the diffusion process diminishes as the scan rate increases due to the limited time for the insertion of ions into the crystal lattice of the nanomaterials.

Based on the obtained results, an increased amount of Co^{2+} is highly beneficial for achieving improved electrochemical performance. The theoretical specific capacitance can be calculated using the formula: $C_{Th} = (n \times F)/(M \times V)$, where *n*, *F*, *M*, and *V* signifies the number of electrons transferred in the electrochemical process, Faraday constant, molar mass of the electroactive material, and operating voltage window, respectively. The theoretical capacitance of metal ions is primarily influenced by the mean number of electrons transferred during the redox reaction, assuming a constant molar mass and operating window. For Co-based compounds, Co^{2+} ions can lose two electrons and be oxidized to Co^{4+} ($n = 2$). However, in the case of $HCoO_2$, cobalt ions lose only one electron and are converted from Co^{3+} to Co^{4+} ($n = 1$). Consequently, the $Co_{1-x}S$ compounds incorporated in the electrode material possess the ability to release two electrons, leading to a significantly higher theoretical capacitance compared to the corresponding $HCoO_2$ compounds. Furthermore, as the Co content increases, the theoretical capacitance of $Co_{1-x}S/HCoO_2$ compounds gradually increases. However, it is crucial to consider the impact of the physical characteristics of the nanomaterial arrays on the practical utilization of this theoretical capacity. The role of uniform and highly interconnected arrays on synthesized electrode is crucial in enhancing the surface area, which in turn enables efficient and improved electrochemical performance. These arrays provide additional active sites for redox reactions, facilitate proper insertion of electrolyte ions into the nanomaterial's pores, and promote enhanced mobility of electrons during the electrochemical process. Optimizing the physical attributes of nanomaterial arrays enables maximum utilization of the theoretical capacity and enhances the overall electrochemical performance [56].

3.2.1 Electrochemical performance of the asymmetric supercapacitor (($Co_{1-x}S/HCoO_2$)-1@Fe_3C/PCNFs// Fe_2O_3/NPC@PCNFs)

To further examine the practical use of the ($Co_{1-x}S/HCoO_2$)-1@Fe_3C/PCNFs electrode, an asymmetric supercapacitor (ASC) is constructed using ($Co_{1-x}S/HCoO_2$)-1@Fe_3C/PCNFs and Fe_2O_3/NPC@PCNFs as the anode and cathode, respectively. The electrochemical performance of Fe_2O_3/NPC@PCNFs (anode) is presented in our previous work [63]. At 1 A g^{-1}, Fe_2O_3/NPC@PCNFs has a maximum specific capacitance of 249 F g^{-1}. To achieve the best electrochemical performance of the ASC device, it is crucial to balance the mass/charge between the cathode and anode during the fabrication process. The mass/charge balance is determined using Eq. S2 (supporting information file). The estimated optimal mass ratio between ($Co_{1-x}S/HCoO_2$)-1@Fe_3C/PCNFs and Fe_2O_3/NPC@PCNFs is estimated to be 1:3.46. Similarly, to optimize the stable voltage, a CV (Fig. S11a) test of the fabricated device is performed in different voltage ranges at a scan rate of 30 mV s^{-1}. The CV curve shape is unchanged and almost overlaps when the voltage increases from 1.0 to 1.5 V. Furthermore, the noticeable dramatic increase in current density in the CV curve at high voltages ranging from 0 to 1.6 V is due to electrolyte decomposition/water splitting, which is not good for the device's long-term stability and ideal cell performance. This fact suggests that the fabricated ASC device can function consistently in the 1.5 V voltage window. The individual CV curves of the cathode ($Co_{1-x}S/HCoO_2$-1@Fe_3C/PCNFs) and anode (Fe_2O_3/NPC@PCNFs) at 30 mV s^{-1} are shown in Fig. 6a. The rate capability of the ASC device is evaluated by cyclic voltammetry at different scan rates within the optimized voltage range (0 to 1.5 V). As illustrated in Fig. 6b, the observed narrow rectangular curve in the low voltage range and broad curve with a distinct redox peak and broadening of the redox peak in the high voltage range are due to the efficacious assembly of ($Co_{1-x}S/HCoO_2$)-1@Fe_3C/PCNFs and Fe_2O_3/NPC@PCNFs in the ASC device. With

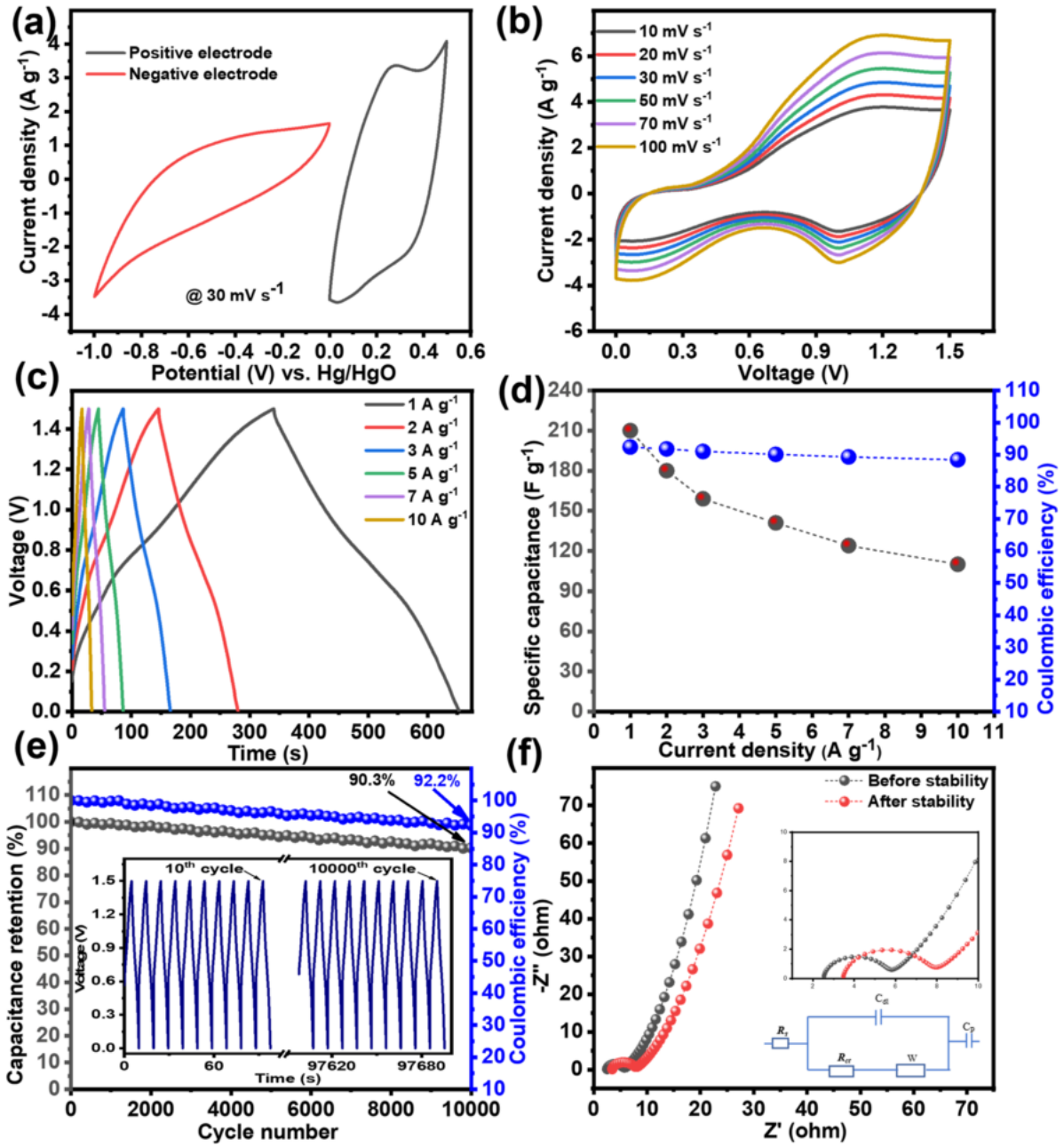

Fig. 6 **a** Individual CV curves of the cathode and anode at 30 mV s^{-1}, **b**, **c** CV and GCD curves of the ASC recorded at various scan rates and different current densities, respectively, **d** specific capacitance and coulombic efficiency of the ASC device at different current densities, **e** capacitance retention and coulombic efficiency of the ASC device over 10,000 GCD cycles (inset: initial and final 10 cycles of 10,000 charge-discharge cycles), and **f** EIS plots of the ASC device before and after 10,000 GCD cycles with an inset equivalent circuit diagram

an increasing scan rate from 10 to 100 mV s^{-1}, the shape of the CV is preserved without noticeable distortion, suggesting the superb rate capability and rapid reaction kinetics of the fabricated hybrid ASC device.

The specific capacitance, energy density, power density, and coulombic efficiency of the ASC are determined by analyzing the galvanostatic discharge curves using Eqs. S3, S4, S5, and S6, as provided in the Supporting information file. These calculations allow for a comprehensive evaluation of the electrochemical performance and energy storage capabilities of the ASC. The charge/discharge curves of the ASC at different current densities within the fixed voltage range, as depicted in Fig. 6c, exhibit nearly symmetric behavior. This indicates excellent

reversibility and high coulombic efficiency of the device. The specific capacitance of the ASC is calculated to be 210 F g^{-1} at a current density of 1 A g^{-1}, demonstrating its favorable energy storage performance. Furthermore, the device retains approximately 52.76% of its initial capacitance even at a higher current density of 10 A g^{-1}, as shown in Fig. 6d. These findings highlight the remarkable capacitance retention capability of the ASC under varying current densities. At a constant current density of 3 A g^{-1}, the GCD curves depicted in Fig. S11b exhibit a range from 0.5 to 1.0 V. These curves demonstrate exceptional overlap and exemplify high coulombic efficiency. The execution of a GCD stability test is crucial for evaluating the long-term cycle life and durability of ASC devices, ensuring their suitability for real-world applications. The initial and final 10 cycles of the cyclic stability test of the ASC at 10 A g^{-1} are depicted in the inset in Fig. 6e. As shown in Fig. 6e, the assembled electrode materials have outstanding as well as impressive cycling performance, retaining almost 90.3% of the initial capacitance with remarkable coulombic efficiency after 10,000 continuous charge-discharge cycles at a current density of 20 A g^{-1}. The EIS test is performed to determine how the fabricated asymmetric supercapacitor device with aqueous electrolyte maintains excellent electrical contact with the least amount of ionic resistance suitable for practical applications. Figure 6f reveals the typical Nyquist plot before and after the cycling stability test. Before the stability test, the fabricated symmetric supercapacitor device exhibits R_s and R_{ct} values of ~ 2.51 and 2.98 Ω, respectively. After 10,000 cycles, the device's R_s and R_{ct} values increase to 3.45 and 4.07 Ω, respectively. However, the slope of the straight line remains nearly the same, indicating that the electrode materials exhibit excellent stability. The remarkable increase in the R_s and R_{ct} values of the electrode material is due to the partial dissolution of $Co_{1-x}S/HCoO_2$, which facilitates rapid ion transport and inhibits the active sites for the faradaic response, resulting in an increase in the semicircle diameter at higher frequencies. The Bode plot in Fig. S11c provides evidence of the favorable electrochemical performance of the fabricated ASC device by demonstrating its low internal resistance, which is indicative of quick ionic diffusion and a partial ideal capacitive behavior or redox nature of ASC [2, 29].

The Ragone plot presented in Fig. 7a depicts the relationship between energy density (E) and power density (P) of the $(Co_{1-x}S/HCoO_2)$-1@Fe_3C/PCNFs//Fe_2O_3/NPC@PCNFs ASC device, providing an evaluation of its practical performance. The fabricated device demonstrates exceptional performance, with a maximum energy density of 65.68 Wh kg^{-1} and a power density of 752.7 W kg^{-1} at a current density of 1 A g^{-1}. Furthermore, it achieves a maximum power density of 7575.94 W kg^{-1} with an energy density of 34.63 Wh kg^{-1} at a current density of 10 A g^{-1}. These values surpass those reported in previous ASC devices, as presented in Table 1. The practical application potential of the device is exemplified by successfully illuminating a red light-emitting diode (LED) using two fabricated devices connected in series, as depicted in Fig. 7b. Additionally, it is evident that the morphology, variety of active sites achieved through double-phase engineering, and low resistivity of the electrode materials significantly impact the performance of the ASC.

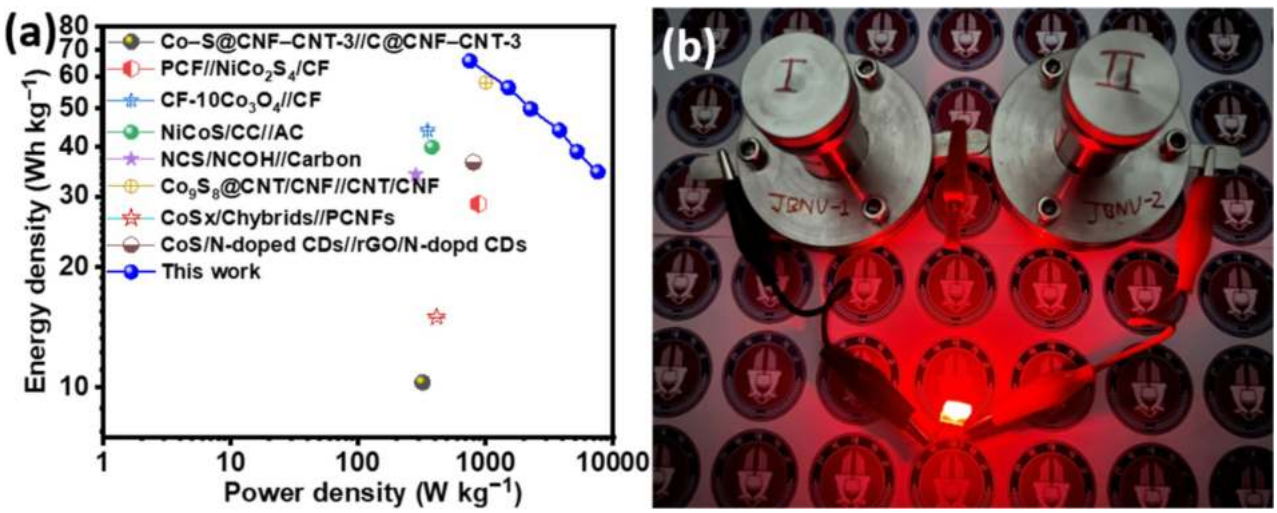

Fig. 7 **a** Ragone plot of the $(Co_{1-x}S/HCoO_2)$-1@Fe_3C/PCNFs//Fe_2O_3/NPC@PCNFs with identical ASC devices and **b** digital photography of a red LED illuminated by two ASC devices connected in series

Table 1 Comparison of identical ASCs with ($Co_{1-x}S/HCoO_2$)-1@Fe_3C/PCNFs//Fe_2O_3/NPC@PCNFs in a 2-electrode system

S. N.	2-electrode ASC devices	Electrolyte	Maximum energy density (Wh kg^{-1}) @ power density (W kg^{-1})	Maximum power density (W kg^{-1}) @ energy density (Wh kg^{-1})	Capacitance retention (after n cycles)	Ref.
1.	Co–S@CNF–CNT-3//C@CNF–CNT-3	3M KOH	10.3 @ 320 at 0.4 A g^{-1}	8000 @ 7.56 at 10 A g^{-1}	96.9% after 10,000 cycles at 5 A g^{-1}	[73]
2.	PCF//$NiCo_2S_4$/CF	2M KOH	28.8 @ 878.3	NA	92% after 5000 cycles @ 10 A g^{-1}	[74]
3.	CF-10Co_3O_4//CF	1M KOH	44 @ 350	NA	NA	[75]
4.	NiCoS/CC//AC	2M KOH	40 @ 379	NA	NA	[76]
5.	NCS/NCOH//Carbon	0.1 M KOH	34.1@ 282.7	2827 @ 16.5	109% after 16,000 cycles @ 0.667 A g^{-1}	[77]
6.	Co_9S_8@CNT/CNF//CNT/CNF	2M KOH	58 @ 1000	16700@ 38	93% after 10,000 cycles @ 5 A g^{-1}	[78]
7.	CoS_x/C hybrids//PCNFs	1M H_2SO_4	15.0 @ 413	8300 @ 6	80% after 2000 cycles @ 0.5 A g^{-1}	[79]
8.	CoS/N-doped CDs//rGO/N-doped CDs	3M KOH	36.6 @ 800	16000 @ 25.6	85.9% after 10,000 cycles at 10 A g^{-1}	[80]
11.	**($Co_{1-x}S/HCoO_2$)-1@Fe_3C/PCNFs//Fe_2O_3/NPC@PCNFs**	**3M KOH**	**65.68 @ 752.7**	**7575.94 @ 34.63**	**90.3% after 10,000 cycles at 20 A g^{-1}**	**This work**

CNFs carbon nanofibers, *NC-CNT* α-$Ni_{1/3}Co_{2/3}(OH)_2$-carbon nanotube, *NCS/NCOH composite* 4$Ni(OH)_2$·NiOOH/Ni_3S_2, *NCF* N-doped carbon foam, *CF* carbon fiber, *PVA* polyvinyl alcohol

4 Conclusions

MIL-88A-integrated PCNFs are used as a substrate for the growth of $Co_{1-x}S/HCoO_2$. The in situ chemical curing process is applied for the successful growth of hexagonal $Co_{1-x}S/HCoO_2$ on Fe_3C/PCNFs. The prepared electrode materials, ($Co_{1-x}S/HCoO_2$)-1@Fe_3C/PCNFs, exhibit excellent electrochemical properties, including fast ion and electron transport, abundant electroactive sites, a large surface area, high electrochemical activity, and good electrical conductivity, enabling effective electrochemical energy storage through reversible faradaic redox reactions. As a result, the ($Co_{1-x}S/HCoO_2$)-1@Fe_3C/PCNFs electrode demonstrates a high specific capacitance value of 1724 F g^{-1} at a current density of 1 A g^{-1} and retains 59.1% of its capacitance even at a high current density of 10 A g^{-1}. The ($Co_{1-x}S/HCoO_2$)-1@Fe_3C/PCNFs electrode material, featuring highly and uniformly connected hexagonal-structured double-phase nanoporous materials, demonstrates excellent rate capability and remarkable cyclic stability, maintaining 89.8% capacity retention over 10,000 cycles. The remarkable electrochemical performance of ($Co_{1-x}S/HCoO_2$)-1@Fe_3C/PCNFs is highly beneficial for the fabrication of ASCs, with a mass ratio of positive and negative electrode materials of 1:3.45, even though the negative electrode (Fe_2O_3/NPC@PCNFs) shows a Cs of 249 F g^{-1} at 1 A g^{-1}. The as-fabricated ASC device ($Co_{1-x}S/HCoO_2$)-1@Fe_3C/PCNFs//Fe_2O_3/NPC@PCNFs) achieves a high energy density of 65.68 Wh kg^{-1} at 752.7 W kg^{-1} at 1.5 V cell voltage, as well as an excellent cycling performance of 90.3% capacitance retention over 10,000 cycles. As a result, this study is likely to inspire the creation of advanced functional electrode materials with improved performance for asymmetric supercapacitor applications.

Supplementary Information The online version contains supplementary material available at https://doi.org/10.1007/s42114-023-00755-9.

Author contribution Debendra Acharya, Kisan Chhetri, and Hak Yong Kim made the concept and methodology of this research. Debendra Acharya wrote and revised the main manuscript text. Roshan Mangal Bhattarai prepared the Schematic diagram (Fig. 1) and edited the main manuscript text. Alagan Muthurasu, Tae Hoon Ko, Taewoo Kim, Syafiqah Saidin, and Jae-Shik Choi analyzed all data. Hak Yong Kim contributed to data analysis and provided funding support. Kisan Chhetri, and Hak Yong Kim supervised this work. All authors reviewed and revised the manuscript.

Funding This study was supported by the National Research Foundation (NRF) of Korea; Korean government (MSIT) project numbers 2019R1A5A8080326 and 2022R1A2C2007676 financially supported this research.

Declarations

Competing interests The authors declare no competing interests.

References

1. Ma Y, Hou C, Kimura H, Xie X, Jiang H, Sun X, Yang X, Zhang Y, Du W (2023) Recent advances in the application of carbon-based electrode materials for high-performance zinc ion capacitors: a mini review. Adv Compos Hybrid Mater 6(2):59. https://doi.org/10.1007/s42114-023-00636-1

2. Ma Y, Xie X, Yang W, Yu Z, Sun X, Zhang Y, Yang X, Kimura H, Hou C, Guo Z, Du W (2021) Recent advances in transition metal oxides with different dimensions as electrodes for high-performance supercapacitors. Adv Compos Hybrid Mater 4(4):906–924. https://doi.org/10.1007/s42114-021-00358-2
3. Dang C, Mu Q, Xie X, Sun X, Yang X, Zhang Y, Maganti S, Huang M, Jiang Q, Seok I, Du W, Hou C (2022) Recent progress in cathode catalyst for nonaqueous lithium oxygen batteries: a review. Adv Compos Hybrid Mater 5(2):606–626. https://doi.org/10.1007/s42114-022-00500-8
4. Zhang Y, Liu L, Zhao L, Hou C, Huang M, Algadi H, Li D, Xia Q, Wang J, Zhou Z, Han X, Long Y, Li Y, Zhang Z, Liu Y (2022) Sandwich-like $CoMoP_2$/MoP heterostructures coupling N, P co-doped carbon nanosheets as advanced anodes for high-performance lithium-ion batteries. Adv Compos Hybrid Mater 5(3):2601–2610. https://doi.org/10.1007/s42114-022-00535-x
5. Hou C, Yang W, Kimura H, Xie X, Zhang X, Sun X, Yu Z, Yang X, Zhang Y, Wang B, Xu BB, Sridhar D, Algadi H, Guo Z, Du W (2023) Boosted lithium storage performance by local build-in electric field derived by oxygen vacancies in 3D holey N-doped carbon structure decorated with molybdenum dioxide. J Mater Sci Technol 142:185–195. https://doi.org/10.1016/j.jmst.2022.10.007
6. Li F, Li Q, Kimura H, Xie X, Zhang X, Wu N, Sun X, Xu BB, Algadi H, Pashameah RA, Alanazi AK, Alzahrani E, Li H, Du W, Guo Z, Hou C (2023) Morphology controllable urchin-shaped bimetallic nickel-cobalt oxide/carbon composites with enhanced electromagnetic wave absorption performance. J Mater Sci Technol 148:250–259. https://doi.org/10.1016/j.jmst.2022.12.003
7. Hou C, Wang B, Murugadoss V, Vupputuri S, Chao Y, Guo Z, Wang C, Du W (2020) Recent advances in Co_3O_4 as anode materials for high-performance lithium-ion batteries. Eng Sci 11:19–30. https://doi.org/10.30919/es8d1128
8. Mu Q, Liu R, Kimura H, Li J, Jiang H, Zhang X, Yu Z, Sun X, Algadi H, Guo Z, Du W, Hou C (2022) Supramolecular self-assembly synthesis of hemoglobin-like amorphous CoP@N, P-doped carbon composites enable ultralong stable cycling under high-current density for lithium-ion battery anodes. Adv Compo Hybrid Mater 6(1):23. https://doi.org/10.1007/s42114-022-00607-y
9. Sheberla D, Bachman JC, Elias JS, Sun C-J, Shao-Horn Y, Dincă M (2017) Conductive MOF electrodes for stable supercapacitors with high areal capacitance. Nat Mater 16(2):220–224. https://doi.org/10.1038/nmat4766
10. Simon P, Gogotsi Y (2008) Materials for electrochemical capacitors. Nat Mater 7(11):845–854. https://doi.org/10.1038/nmat2297
11. Gao X, Dong Y, Li S, Zhou J, Wang L, Wang B (2020) MOFs and COFs for batteries and supercapacitors. Electrochem Energy Rev 3(1):81–126. https://doi.org/10.1007/s41918-019-00055-1
12. Miller JR, Simon P (2008) Electrochemical capacitors for energy management. Science 321(5889):651–652. https://doi.org/10.1126/science.1158736
13. Jain A, Manippady SR, Tang R, Nishihara H, Sobczak K, Matejka V, Michalska M (2022) Vanadium oxide nanorods as an electrode material for solid state supercapacitor. Sci Rep 12(1):21024. https://doi.org/10.1038/s41598-022-25707-z
14. Kim T, Subedi S, Dahal B, Chhetri K, Mukhiya T, Muthurasu A, Gautam J, Lohani PC, Acharya D, Pathak I, Chae S-H, Ko TH, Kim HY (2022) Homogeneous elongation of N-doped CNTs over nano-fibrillated hollow-carbon-nanofiber: mass and charge balance in asymmetric supercapacitors is no longer problematic. Adv Sci 9(20):2200650. https://doi.org/10.1002/advs.202200650
15. Horn M, MacLeod J, Liu M, Webb J, Motta N (2019) Supercapacitors: a new source of power for electric cars? Econ Anal Policy 61:93–103. https://doi.org/10.1016/j.eap.2018.08.003
16. Li Q, Zhang Q, Sun J, Liu C, Guo J, He B, Zhou Z, Man P, Li C, Xie L, Yao Y (2019) All hierarchical core–shell heterostructures as novel binder-free electrode materials for ultrahigh-energy-density wearable asymmetric supercapacitors. Adv Sci 6(2):1801379. https://doi.org/10.1002/advs.201801379
17. Zhao X, Tao K, Han L (2022) Self-supported metal–organic framework-based nanostructures as binder-free electrodes for supercapacitors. Nanoscale 14(6):2155–2166. https://doi.org/10.1039/D1NR08284A
18. Ko Y, Kwon M, Bae WK, Lee B, Lee SW, Cho J (2017) Flexible supercapacitor electrodes based on real metal-like cellulose papers. Nat Commun 8(1):536. https://doi.org/10.1038/s41467-017-00550-3
19. Bhattarai RM, Chhetri K, Natarajan S, Saud S, Kim SJ, Mok YS (2022) Activated carbon derived from cherry flower biowaste with a self-doped heteroatom and large specific surface area for supercapacitor and sodium-ion battery applications. Chemosphere 303:135290. https://doi.org/10.1016/j.chemosphere.2022.135290
20. Zhao Y, Liu F, Zhu K, Maganti S, Zhao Z, Bai P (2022) Three-dimensional printing of the copper sulfate hybrid composites for supercapacitor electrodes with ultra-high areal and volumetric capacitances. Adv Compos Hybrid Mater 5(2):1537–1547. https://doi.org/10.1007/s42114-022-00430-5
21. Gautam KP, Acharya D, Bhatta I, Subedi V, Das M, Neupane S, Kunwar J, Chhetri K, Yadav AP (2022) Nickel oxide-incorporated polyaniline nanocomposites as an efficient electrode material for supercapacitor application. Inorganics 10(6):86
22. Xie Y (2022) Electrochemical and hydrothermal activation of carbon fiber supercapacitor electrode. Fibers and Polym 23(1):10–17. https://doi.org/10.1007/s12221-021-0059-1
23. Asare K, Hasan MF, Shahbazi A, Zhang L (2021) A comparative study of porous and hollow carbon nanofibrous structures from electrospinning for supercapacitor electrode material development. Surf Interfaces 26:101386. https://doi.org/10.1016/j.surfin.2021.101386
24. Zhu M, Liu H, Cao Q, Zheng H, Xu D, Guo H, Wang S, Li Y, Zhou J (2020) Electrospun lignin-based carbon nanofibers as supercapacitor electrodes. ACS Sustain Chem Eng 8(34):12831–12841. https://doi.org/10.1021/acssuschemeng.0c03062
25. Ojha GP, Pant B, Acharya J, Lohani PC, Park M (2023) Solvothermal-localized selenylation transformation of cobalt nickel MOFs templated heterointerfaces enriched monoclinic Co_3Se_4/$CoNi_2Se_4$@ activated knitted carbon cloth for flexible and bi-axial stretchable supercapacitors. Chem Eng J 464:142621. https://doi.org/10.1016/j.cej.2023.142621
26. Acharya D, Pathak I, Muthurasu A, Bhattarai RM, Kim T, Ko TH, Saidin S, Chhetri K, Kim HY (2023) In situ transmogrification of nanoarchitectured Fe-MOFs decorated porous carbon nanofibers into efficient positrode for asymmetric supercapacitor application. J Energy Storage 63:106992. https://doi.org/10.1016/j.est.2023.106992
27. Kumar S, Saeed G, Zhu L, Hui KN, Kim NH, Lee JH (2021) 0D to 3D carbon-based networks combined with pseudocapacitive electrode material for high energy density supercapacitor: a review. Chem Eng J 403:126352. https://doi.org/10.1016/j.cej.2020.126352
28. Liang J, Zhao H, Yue L, Fan G, Li T, Lu S, Chen G, Gao S, Asiri Abdullah M, Sun X (2020) Recent advances in electrospun nanofibers for supercapacitors. J Mater Chem A 8(33):16747–16789. https://doi.org/10.1039/D0TA05100D
29. Lai C, Guo Y, Zhao H, Song H, Qu X, Huang M, Hong SW, Lee K (2022) High-performance double "ion-buffering reservoirs" of asymmetric supercapacitors enabled by battery-type hierarchical porous sandwich-like Co_3O_4 and 3D graphene aerogels. Adv Compos Hybrid Mater 5(3):2557–2574. https://doi.org/10.1007/s42114-022-00532-0
30. Vinodh R, Gopi CVVM, Kummara VGR, Atchudan R, Ahamad T, Sambasivam S, Yi M, Obaidat IM, Kim H-J (2020) A review

on porous carbon electrode material derived from hypercross-linked polymers for supercapacitor applications. J Energy Storage 32:101831. https://doi.org/10.1016/j.est.2020.101831
31. Liu Y, Liu Q, Wang L, Yang X, Yang W, Zheng J, Hou H (2020) Advanced supercapacitors based on porous hollow carbon nanofiber electrodes with high specific capacitance and large energy density. ACS Appl Mater Interfaces 12(4):4777–4786. https://doi.org/10.1021/acsami.9b19977
32. Chhetri K, Kim T, Acharya D, Muthurasu A, Dahal B, Bhattarai RM, Lohani PC, Pathak I, Ji S, Ko TH, Kim HY (2022) Hollow carbon nanofibers with inside-outside decoration of bi-metallic MOF derived Ni-Fe phosphides as electrode materials for asymmetric supercapacitors. Chem Eng J 450:138363. https://doi.org/10.1016/j.cej.2022.138363
33. Baig MM, Gul IH, Baig SM, Shahzad F (2022) 2D MXenes: Synthesis, properties, and electrochemical energy storage for supercapacitors – a review. J Electroanal Chem 904:115920. https://doi.org/10.1016/j.jelechem.2021.115920
34. Poudel MB, Kim HJ (2022) Confinement of Zn-Mg-Al-layered double hydroxide and α-Fe_2O_3 nanorods on hollow porous carbon nanofibers: a free-standing electrode for solid-state symmetric supercapacitors. Chem Eng J 429:132345. https://doi.org/10.1016/j.cej.2021.132345
35. Wang J, Huang Y, Gao Y, Dai J, Sun X (2022) The construction of carbon nanofiber composites modified by graphene/polypyrrole for flexible supercapacitors. J Energy Storage 51:104581. https://doi.org/10.1016/j.est.2022.104581
36. Pathak I, Acharya D, Chhetri K, Chandra Lohani P, Subedi S, Muthurasu A, Kim T, Ko TH, Dahal B, Kim HY (2023) Ti3C2Tx MXene embedded metal–organic framework-based porous electrospun carbon nanofibers as a freestanding electrode for supercapacitors. J Mater Chem A 11(10):5001–5014. https://doi.org/10.1039/D2TA09726E
37. Gao H, Shen H, Wu H, Jing H, Sun Y, Liu B, Chen Z, Song J, Lu L, Wu Z, Hao Q (2021) Review of pristine metal–organic frameworks for supercapacitors: recent progress and perspectives. Energy Fuels 35(16):12884–12901. https://doi.org/10.1021/acs.energyfuels.1c01722
38. Xu B, Zhang H, Mei H, Sun D (2020) Recent progress in metal-organic framework-based supercapacitor electrode materials. Coord Chem Rev 420:213438. https://doi.org/10.1016/j.ccr.2020.213438
39. Cherusseri J, Pandey D, Sambath Kumar K, Thomas J, Zhai L (2020) Flexible supercapacitor electrodes using metal–organic frameworks. Nanoscale 12(34):17649–17662. https://doi.org/10.1039/D0NR03549A
40. Wang D-G, Liang Z, Gao S, Qu C, Zou R (2020) Metal-organic framework-based materials for hybrid supercapacitor application. Coord Chem Rev 404:213093. https://doi.org/10.1016/j.ccr.2019.213093
41. Chhetri K, Muthurasu A, Dahal B, Kim T, Mukhiya T, Chae SH, Ko TH, Choi YC, Kim HY (2022) Engineering the abundant heterointerfaces of integrated bimetallic sulfide-coupled 2D MOF-derived mesoporous CoS_2 nanoarray hybrids for electrocatalytic water splitting. Mater Today Nano 17:100146. https://doi.org/10.1016/j.mtnano.2021.100146
42. Liang Z, Zhao R, Qiu T, Zou R, Xu Q (2019) Metal-organic framework-derived materials for electrochemical energy applications. EnergyChem 1(1):100001. https://doi.org/10.1016/j.enchem.2019.100001
43. Guan BY, Yu XY, Wu HB, Lou XW (2017) Complex nanostructures from materials based on metal–organic frameworks for electrochemical energy storage and conversion. Adv Mater 29(47):1703614. https://doi.org/10.1002/adma.201703614
44. Du R, Wu Y, Yang Y, Zhai T, Zhou T, Shang Q, Zhu L, Shang C, Guo Z (2021) Porosity engineering of MOF-based materials for electrochemical energy storage. Adv Energy Mater 11(20):2100154. https://doi.org/10.1002/aenm.202100154
45. Wang C, Kaneti YV, Bando Y, Lin J, Liu C, Li J, Yamauchi Y (2018) Metal–organic framework-derived one-dimensional porous or hollow carbon-based nanofibers for energy storage and conversion. Mater Horiz 5(3):394–407. https://doi.org/10.1039/C8MH00133B
46. Acharya D, Muthurasu A, Ko TH, Bhattarai RM, Kim T, Chae S-H, Saidin S, Chhetri K, Kim HY (2023) Iron MOF-derived Fe_2O_3/NPC decorated on MIL-88A converted Fe_3C implanted electrospun porous carbon nanofibers for symmetric supercapacitors. ACS Appl Energy Mater. https://doi.org/10.1021/acsaem.3c00567
47. Schoetz T, Gordon LW, Ivanov S, Bund A, Mandler D, Messinger RJ (2022) Disentangling faradaic, pseudocapacitive, and capacitive charge storage: a tutorial for the characterization of batteries, supercapacitors, and hybrid systems. Electrochimica Acta 412:140072. https://doi.org/10.1016/j.electacta.2022.140072
48. Yang W, Peng D, Kimura H, Zhang X, Sun X, Pashameah RA, Alzahrani E, Wang B, Guo Z, Du W, Hou C (2022) Honeycomb-like nitrogen-doped porous carbon decorated with Co_3O_4 nanoparticles for superior electrochemical performance pseudo-capacitive lithium storage and supercapacitors. Adv Compos Hybrid Mater 5(4):3146–3157. https://doi.org/10.1007/s42114-022-00556-6
49. Bhattarai RM, Chhetri K, Saud S, Teke S, Kim SJ, Mok YS (2022) Eco-friendly synthesis of cobalt molybdenum hydroxide 3d nanostructures on carbon fabric coupled with cherry flower waste-derived activated carbon for quasi-solid-state flexible asymmetric supercapacitors. ACS Appl Nano Mater 5(1):160–175. https://doi.org/10.1021/acsanm.1c02354
50. Gao M, Li Y, Yang J, Liu Y, Liu Y, Zhang X, Wu S, Cai K (2022) Nickel-cobalt (oxy)hydroxide battery-type supercapacitor electrode with high mass loading. Chem Eng J 429:132423. https://doi.org/10.1016/j.cej.2021.132423
51. Kandel MR, Pan UN, Dhakal PP, Ghising RB, Nguyen TT, Zhao J, Kim NH, Lee JH (2023) Unique heterointerface engineering of Ni_2P−MnP nanosheets coupled Co_2P nanoflowers as hierarchical dual-functional electrocatalyst for highly proficient overall water-splitting. Appl Catal B: Environ 331:122680. https://doi.org/10.1016/j.apcatb.2023.122680
52. Gao Y, Zhao L (2022) Review on recent advances in nanostructured transition-metal-sulfide-based electrode materials for cathode materials of asymmetric supercapacitors. Chem Eng J 430:132745. https://doi.org/10.1016/j.cej.2021.132745
53. Liang H, Lin T, Wang S, Jia H, Li C, Cao J, Feng J, Fei W, Qi J (2020) A free-standing manganese cobalt sulfide@cobalt nickel layered double hydroxide core–shell heterostructure for an asymmetric supercapacitor. Dalton Trans 49(1):196–202. https://doi.org/10.1039/C9DT03974K
54. Huang J, Xie Y, You Y, Yuan J, Xu Q, Xie H, Chen Y (2023) Rational design of electrode materials for advanced supercapacitors: from lab research to commercialization. Adv Func Mater 33(14):2213095. https://doi.org/10.1002/adfm.202213095
55. Bhattarai RM, Chhetri K, Le N, Acharya D, Saud S, Nguyen MCHPL, Kim SJ, Mok YS (2023) Oxygen functionalization-assisted anionic exchange toward unique construction of flower-like transition metal chalcogenide embedded carbon fabric for ultra-long life flexible energy storage and conversion. Carbon Energy n/a(n/a):e392. https://doi.org/10.1002/cey2.392
56. Chen H, Jiang J, Zhao Y, Zhang L, Guo D, Xia D (2015) One-pot synthesis of porous nickel cobalt sulphides: tuning the composition for superior pseudocapacitance. J Mater Chem A 3(1):428–437. https://doi.org/10.1039/C4TA04420G
57. Tiwari AP, Chhetri K, Kim H, Ji S, Chae S-H, Kim T, Kim HY (2021) Self-assembled polypyrrole hierarchical porous networks as the cathode and porous three dimensional carbonaceous

networks as the anode materials for asymmetric supercapacitor. J Energy Storage 33:102080. https://doi.org/10.1016/j.est.2020.102080
58. Wei C, Sun J, Zhang Y, Liu Y, Guo Z, Du W, Liu L, Zhang Y (2022) Hierarchical $Ni(OH)_2$–MnO_2 hollow spheres as an electrode material for high-performance supercapacitors. Inorg Chem Front 9(14):3542–3551. https://doi.org/10.1039/D2QI00780K
59. Zhou Q, Li W, Xu H, Gao M, Dong X, Lin J (2022) Fabrication of hierarchical integrated 3D hollow MnS@MoS_2 microcubes via a template-controlled synthesis for asymmetric supercapacitors. J Mater Chem A 10(17):9370–9379. https://doi.org/10.1039/D2TA00106C
60. Saraf M, Rajak R, Mobin SM (2019) MOF derived high surface area enabled porous Co_3O_4 nanoparticles for supercapacitors. ChemistrySelect 4(27):8142–8149. https://doi.org/10.1002/slct.201901652
61. Liu Y, Xu X, Shao Z, Jiang SP (2020) Metal-organic frameworks derived porous carbon, metal oxides and metal sulfides-based compounds for supercapacitors application. Energy Stor Mater 26:1–22. https://doi.org/10.1016/j.ensm.2019.12.019
62. Justin Raj C, Kim BC, Cho W-J, Park S, Jeong HT, Yoo K, Yu KH (2015) Rapid hydrothermal synthesis of cobalt oxyhydroxide nanorods for supercapacitor applications. J Electroanal Chem 747:130–135. https://doi.org/10.1016/j.jelechem.2015.04.013
63. Acharya D, Pathak I, Dahal B, Lohani PC, Bhattarai RM, Muthurasu A, Kim T, Ko TH, Chhetri K, Kim HY (2023) Immoderate nanoarchitectures of bimetallic MOF derived Ni–Fe–O/NPC on porous carbon nanofibers as freestanding electrode for asymmetric supercapacitors. Carbon 201:12–23. https://doi.org/10.1016/j.carbon.2022.08.091
64. Lin Q, Guo D, Zhou L, Yang L, Jin H, Li J, Fang G, Xa C, Wang S (2022) Tuning the interface of $Co_{1-x}S$/Co(OH)F by atomic replacement strategy toward high-performance electrocatalytic oxygen evolution. ACS Nano 16(9):15460–15470. https://doi.org/10.1021/acsnano.2c07588
65. Xu H, Ye K, Zhu K, Yin J, Yan J, Wang G, Cao D (2020) Template-directed assembly of urchin-like CoS_x/Co-MOF as an efficient bifunctional electrocatalyst for overall water and urea electrolysis. Inorg Chem Front 7(14):2602–2610. https://doi.org/10.1039/D0QI00408A
66. Guan X, Huang M, Yang L, Wang G, Guan X (2019) Facial design and synthesis of CoS_x/Ni-Co LDH nanocages with rhombic dodecahedral structure for high-performance asymmetric supercapacitors. Chem Eng J 372:151–162. https://doi.org/10.1016/j.cej.2019.04.145
67. Zheng G, Wu C, Wang J, Mo S, Zou Z, Zhou B, Long F (2019) Space-confined effect one-pot synthesis of γ-AlO(OH)/MgAl-LDH heterostructures with excellent adsorption performance. Nanoscale Res Lett 14(1):281. https://doi.org/10.1186/s11671-019-3112-x
68. Greczynski G, Hultman L (2021) The same chemical state of carbon gives rise to two peaks in X-ray photoelectron spectroscopy. Sci Rep 11(1):11195. https://doi.org/10.1038/s41598-021-90780-9
69. Wu K, Hu Y, Cheng Z, Pan P, Zhang M, Jiang L, Mao J, Ni C, Zhang Y, Wang Z, Gu X, Zhang X (2020) Fe_3C composite carbon nanofiber interlayer for efficient trapping and conversion of polysulfides in lithium-sulfur batteries. J Alloys Compd 847:156443. https://doi.org/10.1016/j.jallcom.2020.156443
70. Mosch HLKS, Akintola O, Plass W, Höppener S, Schubert US, Ignaszak A (2016) Specific surface versus electrochemically active area of the carbon/polypyrrole capacitor: correlation of ion dynamics studied by an electrochemical quartz crystal microbalance with BET surface. Langmuir 32(18):4440–4449. https://doi.org/10.1021/acs.langmuir.6b00523
71. Wulfert-Holzmann P, Settelein J, Giffin GA (2021) Influence of the specific surface area of Stöber silica additives on the electrochemical properties of negative electrodes in lead-acid batteries. J Energy Storage 34:102193. https://doi.org/10.1016/j.est.2020.102193
72. Jagadale AD, Dubal DP, Lokhande CD (2012) Electrochemical behavior of potentiodynamically deposited cobalt oxyhydroxide (CoOOH) thin films for supercapacitor application. Mater Res Bull 47(3):672–676. https://doi.org/10.1016/j.materresbull.2011.12.029
73. Yao M, Guo C, Zhang Y, Zhao X, Wang Y (2022) In situ encapsulation of metal sulfide into hierarchical nanostructured electrospun nanofibers as self-supported electrodes for flexible quasi-solid-state supercapacitors. J Mater Chem C 10(2):542–548. https://doi.org/10.1039/D1TC03856G
74. Ma Z, Sun Z, Jiang H, Li F, Wang Q, Qu F (2020) Nanoporous electrospun $NiCo_2S_4$ embedded in carbon fiber as an excellent electrode for high-rate supercapacitors. Appl Surf Sci 533:147521. https://doi.org/10.1016/j.apsusc.2020.147521
75. Sharma A, Kumar R, Muchhala D, Shafeeq M, Dwivedi N, Gupta G, Mondal DP (2022) A new approach to in-situ Co_3O_4 nanostructure decorated free-standing carbon foam derived from phenolic resin for high-performance supercapacitor. Mater Today Commun 33:104250. https://doi.org/10.1016/j.mtcomm.2022.104250
76. Liu T, Liu J, Zhang L, Cheng B, Yu J (2020) Construction of nickel cobalt sulfide nanosheet arrays on carbon cloth for performance-enhanced supercapacitor. J Mater Sci Technol 47:113–121. https://doi.org/10.1016/j.jmst.2019.12.027
77. Xiong X, Chen J, Zhang D, Li A, Zhang J, Zeng X (2019) Heterostructured nanocomposites of Ni/co/O/S for high-performance pseudo-supercapacitors. Electrochimica Acta 299:298–311. https://doi.org/10.1016/j.electacta.2018.12.178
78. Zhou Y, Zhu Y, Xu B, Zhang X (2019) High electroactive material loading on a carbon nanotube/carbon nanofiber as an advanced free-standing electrode for asymmetric supercapacitors. Chem Commun 55(28):4083–4086. https://doi.org/10.1039/C9CC01277J
79. Liu Y, Zhou J, Fu W, Zhang P, Pan X, Xie E (2017) In situ synthesis of CoS_x@carbon core-shell nanospheres decorated in carbon nanofibers for capacitor electrodes with superior rate and cycling performances. Carbon 114:187–197. https://doi.org/10.1016/j.carbon.2016.12.018
80. Ji Z, Li N, Xie M, Shen X, Dai W, Liu K, Xu K, Zhu G (2020) High-performance hybrid supercapacitor realized by nitrogen-doped carbon dots modified cobalt sulfide and reduced graphene oxide. Electrochimica Acta 334:135632. https://doi.org/10.1016/j.electacta.2020.135632